International Journal of Solids and Structures 130–131 (2018) 36–48

Contents lists available at ScienceDirect

International Journal of Solids and Structures

journal homepage: www.elsevier.com/locate/ijsolstr

Simulation of micro-scale shear bands using peridynamics with an adaptive dynamic relaxation method

J. Luo[a,*], A. Ramazani[b], V. Sundararaghavan[b]

[a] Department of Mechanical Engineering, University of Michigan, Ann Arbor, MI 48109, USA
[b] Department of Aerospace Engineering, University of Michigan, 1320 Beal Ave, Ann Arbor, MI 48109, USA

ARTICLE INFO

Article history:
Received 1 July 2017
Revised 10 October 2017
Available online 18 October 2017

Keywords:
Microstructure
Crystal plasticity
Peridynamics
Dynamic method
Simulation

ABSTRACT

A peridynamic (PD) implementation of crystal plasticity with an adaptive dynamic relaxation method is presented. Non-ordinary state-based peridynamics and the Newmark's dynamic method with artificial damping are employed to capture strain localizations in polycrystalline microstructures based on a rate-independent crystal plasticity model. Numerical simulations for planar polycrystals are conducted under plane strain pure shear and compression, respectively. The computational efficiency of the explicit PD model is demonstrated to be superior to an implicit PD model for modeling crystal plasticity. The stress field distribution, texture formation, and homogenized stress-strain response predicted by the finite element method and the new dynamic PD model are compared. Finer localization bands are observed in the latter model. The origin and evolution of these shear bands are studied by PD simulations during deformation of three polycrystals with different orientation distributions. Emphasis is placed on the accuracy and efficiency of the adaptive dynamic relaxation method working with crystal plasticity PD models.

1. Introduction

Modeling mechanical behaviors of advanced alloys applied in industrial applications is a persistent and active challenge (Ramazani et al., 2016; Abuzaid et al., 2013; Sun and Sundararaghavan, 2014). One popular numerical model for polycrystalline materials is the crystal plasticity finite element (CPFE) model (Sun and Sundararaghavan, 2014; Roters et al., 2010; Anand and Kothari, 1996) which provides a link between the dislocation-level physics and macro-scale continuum response (Lim et al., 2015). In CPFE models, grains are discretized into finite elements where the crystal plasticity formulations are applied to compute mechanical responses (e.g., stress and strain), crystallographic slip, and reorientation of grains (texturing) at the grain scale (Lim et al., 2015; Roters et al., 2011). However, it is difficult for CPFE models to properly predict strain localizations, in the form of fine shear bands, which have been observed by number of recent experiments (Chen et al., 2017; Khadyko et al., 2016; Pokharel et al., 2014; Kammers and Daly, 2013; Guery et al., 2016). An example of shear band formation in a polycrystal is shown in Fig. 1. The size of shear bands and magnitude of shear computed by standard finite element methods are highly determined by the element size used in the discretization (Pokharel et al., 2014; Kuroda, 2011; Borst et al., 1993).

Considering this disadvantage of CPFE models, different approaches such as non-local constitutive models Evers et al. (2004), higher-gradient models (Menzel and Steinmann, 2000), meshfree methods (Li et al., 2000) have been proposed. Peridynamics, introduced as an alternative integral formulation for continuum mechanics (Silling, 2000), is a particle-based approach capable of handling the formation and propagation of discontinuities. This non-local method, represented by a set of interacting particles, calculates strain at a particle by tracking the motion of surrounding particles. A generalized state-based PD model was later proposed by Silling et al. (2007), in which forces between particles are found using stress tensors obtained from classical constitutive formulations, such as crystal plasticity theory. Recent results based on a crystal plasticity peridynamic (CPPD) model with an implicit Newton–Raphson solver have shown advantages of capturing finer shear bands in planar polycrystals (Sun and Sundararaghavan, 2014).

Implicit methods are traditionally favored compared to explicit dynamic methods for their accuracy at larger time steps (Harewood and McHugh, 2007). However, for crystal plasticity, the computation cost of calculating the tangent modulus matrix is high (Roters et al., 2010). Hence, the new contribution of this paper is a fully explicit implementation of state-based peridynamics for modeling quasi-static deformation of polycrystals. An adaptive dynamic

* Corresponding author.
E-mail addresses: jiangyi@umich.edu (J. Luo), ramazani@umich.edu, ramazani_mat@yahoo.com (A. Ramazani).

https://doi.org/10.1016/j.ijsolstr.2017.10.019
0020-7683/

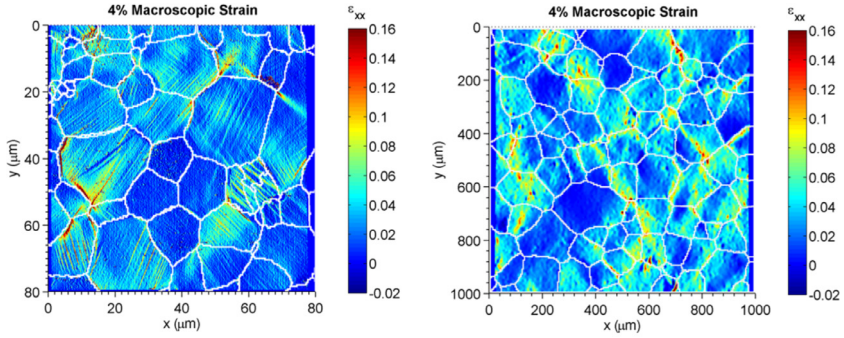

(a) (b)

Fig. 1. Tensile strain maps of a magnesium alloy microstructure for two different heat treatments. Experiment data is obtained using the micro-scale digital image correlation technique (Kammers and Daly, 2013). Fine shear bands due to strain localizations are observed in (a).

relaxation method for quasi-static PD simulations as proposed by Kilic and Madenci (2010) is introduced, where an artificial damping ratio estimated from Rayleigh's quotient is selected to dampen the system leading to a steady-state solution. The critical time step is approximated by a numerical analysis of hyperbolic partial differential equations. Accuracy and effectiveness of this new dynamic CPPD model will be demonstrated with numerical examples.

Although peridynamics has been proven powerful in predicting discontinuities and damages (Madenci and Oterkus, 2014; Gerstle, 2015), it still has some intrinsic numerical issues, among which are zero-energy modes and non-trivial treatment of boundary conditions (Breitenfeld et al., 2014; Tupek and Radovitzky, 2014; Wu and Ben, 2015). Recently, different techniques have been applied. For instance, artificial forces are introduced to reduce spurious modes (Breitenfeld et al., 2014); a stabilized PD formulation with mixed local and nonlocal gradient approximations by Wu and Ben (2015) to enhance essential boundary conditions. Moreover, a peridynamic differential operator extending high-order derivatives to their nonlocal forms has been lately proposed by Madenci et al. (2016). Nevertheless, no uniform and standard scheme is employed coefficients or formulations are chosen on a case-by-case basis. With respect to the PD stability issues, simulations in this paper will mostly adopt the smallest horizon radius to better compare with a continuum local CPFE formulation. One special case with an increased horizon length is conducted in a compression test to better analyze the effect of horizon size on characteristic microstructural length scales. Besides, quantities such as deformation gradients are adjusted for smaller horizons at boundary particles in our model.

In the current work, we conduct simulations for planar polycrystalline microstructures under plane strain pure shear and compression, respectively. The numerical efficiency of the explicit method is compared against the previously proposed implicit CPPD method (Sun and Sundararaghavan, 2014) in the case of pure shear. The stress field distribution, texture formation, and homogenized stress-strain response predicted by the classical CPFE model and the new dynamic CPPD model are compared afterwards. In addition, we perform compression tests of three polycrystals with different orientation distributions to study the nature of localization bands identified from the dynamic CPPD method. Section 2 of this paper provides formulations of state-based peridynamics, the adaptive dynamic relaxation method, and their numerical discretization schemes. The crystal plasticity constitutive model and its numerical implementations are given in Section 3. Section 4 compares planar simulations obtained by the explicit dynamic CPPD model with CPFE results, to demonstrate the capability of the new model for capturing finer shear bands in grains. In the last section, a brief summary and some expectations for the future explicit dynamic CPPD model are discussed.

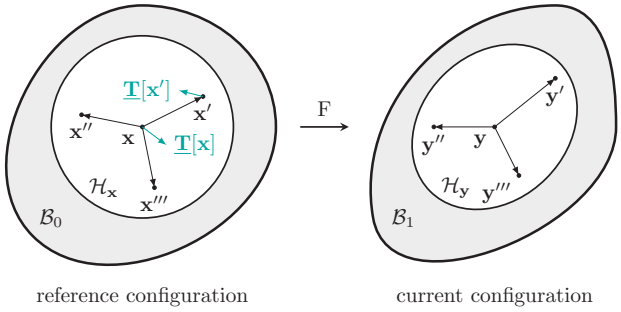

Fig. 2. Kinematics of peridynamics: Particle $\mathbf{x}$ is bonded to all particles ($\mathbf{x}'$, $\mathbf{x}''$, and $\mathbf{x}'''$) within a region $\mathcal{H}_{\mathbf{x}}$. After deformation, particle $\mathbf{x}$ maps to particle $\mathbf{y}$ and the process can be described by an averaged deformation gradient $\mathbf{F}$. $\underline{\mathbf{T}}[\mathbf{x}] = \underline{\mathbf{T}}[\mathbf{x}, t]\langle \mathbf{x}' - \mathbf{x}\rangle$ and $\underline{\mathbf{T}}[\mathbf{x}'] = \underline{\mathbf{T}}[\mathbf{x}', t]\langle \mathbf{x} - \mathbf{x}'\rangle$ are force vector states in the reference configuration at particle $\mathbf{x}$ and $\mathbf{x}'$, respectively. In the non-ordinary state-based PD theory, these two force vector states are not necessarily parallel and can be obtained from the classical stress tensor.

2. Peridynamics with an explicit dynamic solver

2.1. State-based peridynamics

The state-based PD model is first presented by (Silling et al., 2007) in 2007, which is a nonlocal integral reformulation of the continuum theory. Consider a material point $\mathbf{x}$ in the reference configuration which can only interact with its neighboring points $\mathbf{x}'$ in a self-center horizon $\mathcal{H}_{\mathbf{x}}$ with a finite radius δ. Given a displacement field $\mathbf{u}$, the current configuration is then represented by $\mathbf{y} = \mathbf{x} + \mathbf{u}$. Let the initial physical domain be $\mathcal{B}_0$ at time $t = 0$ while $\mathcal{B}_1$ is the deformed domain (shown in Fig. 2).

With the introduction of the *deformation vector state* $\underline{\mathbf{Y}} = \underline{\mathbf{Y}}[\mathbf{x}, t]\langle \mathbf{x}' - \mathbf{x}\rangle = \mathbf{y}' - \mathbf{y}$, which denotes the deformed state of the bond $\xi = \mathbf{x}' - \mathbf{x}$, the deformation gradient $\mathbf{F}$ at particle $\mathbf{x}$ is reformulated as a nonlocal integration over the horizon:

$$\mathbf{F} = \left(\int_{\mathcal{H}_{\mathbf{x}}} \omega(\underline{\mathbf{Y}} \otimes \xi) dV_{\mathbf{x}'}\right)\mathbf{K}^{-1}, \tag{1}$$

where ω is an *influence function* defined at particle $\mathbf{x}$ in $\mathcal{H}_{\mathbf{x}}$. It weights the influence of each neighbor $\mathbf{x}'$ on the particle $\mathbf{x}$ and can be selected as a spherical function based on the initial bond length, i.e., $\omega = \omega(|\xi|)$. $\mathbf{K}$ is a symmetric shape tensor at particle $\mathbf{x}$, defined as

$$\mathbf{K} = \int_{\mathcal{H}_{\mathbf{x}}} \omega(\xi \otimes \xi) dV_{\mathbf{x}'}. \tag{2}$$

Finally, the equation of motion of state-based peridynamics at time t is

$$\rho\ddot{\mathbf{u}}(\mathbf{x},t)=\mathbf{L}(\mathbf{x},t)+\mathbf{b}(\mathbf{x},t),$$
$$\mathbf{L}(\mathbf{x},t)=\int_{\mathcal{H}}\{\underline{\mathbf{T}}[\mathbf{x},t]\langle\mathbf{x}'-\mathbf{x}\rangle-\underline{\mathbf{T}}[\mathbf{x}',t]\langle\mathbf{x}-\mathbf{x}'\rangle\}dV_{\mathbf{x}'}, \tag{3}$$

where $\underline{\mathbf{T}}[\mathbf{x},t]\langle\mathbf{x}'-\mathbf{x}\rangle$ is *the force vector state* operating on the bond $\xi=\mathbf{x}'-\mathbf{x}$ at particle $\mathbf{x}$ at time t and $\mathbf{b}(\mathbf{x},t)$ is the body force. In connection to the classical continuum theory, the force state $\underline{\mathbf{T}}$ can be obtained from the first Piola–Kirchhoff stress, $\mathbf{P}$, at particle $\mathbf{x}$ as follows (Silling et al., 2007):

$$\underline{\mathbf{T}}[\mathbf{x},t]\langle\mathbf{x}'-\mathbf{x}\rangle=\omega\mathbf{P}\mathbf{K}^{-1}\xi. \tag{4}$$

The constitutive model, $\mathbf{P}=\mathcal{F}(\mathbf{F})$, applied in this paper is a rate-independent crystal plasticity model (Anand and Kothari, 1996), which will be elaborated in Section 3. It is worth noting that the balance of angular momentum is ensured with (4) and derivation details can be seen in Silling et al. (2007).

2.2. The adaptive dynamic relaxation method

Since there are no large-matrix operations in the explicit method (e.g., computing the tangent modulus $\partial\mathbf{P}/\partial\mathbf{F}$), less computation cost compared to implicit solvers is foreseeable. In this paper, an explicit dynamic relaxation method with the quasi-static assumption is adopted, in which every time step is selected carefully.

In dynamic methods, a nonlinear problem can be solved through artificial damping leading to a stable solution after a large number of iterations. With the body force ignored, the equation of motion (3) can be rewritten in a vector form as

$$\ddot{\mathbf{u}}(\mathbf{x},t)+c\dot{\mathbf{u}}(\mathbf{x},t)=\mathbf{f}(\mathbf{u},\mathbf{x},t), \tag{5}$$

where c is the damping ratio coefficient and the force vector $\mathbf{f}$ on the right side is defined as $\mathbf{f}(\mathbf{u},\mathbf{x},t)=\mathbf{\Lambda}^{-1}\mathbf{L}(\mathbf{x},t)$, in which $\mathbf{\Lambda}$ is the *fictitious diagonal density matrix*. Based on the adaptive dynamic relaxation method, the most desired diagonal density matrix and damping coefficient can be determined by Greschgorin's theorem and Rayleigh's quotient, respectively (Kilic and Madenci, 2010).

Let $\mathbf{u}^n$, $\dot{\mathbf{u}}^n$, $\ddot{\mathbf{u}}^n$, and $\mathbf{f}^n$ denote the displacement, velocity, acceleration, and force vector field at $t=n$, respectively, and Δt be the time step size assumed constant. In the central difference scheme, the velocity and acceleration vectors are approximated as

$$\dot{\mathbf{u}}^n\approx\frac{1}{2\Delta t}(\mathbf{u}^{n+1}-\mathbf{u}^{n-1}), \tag{6}$$

$$\ddot{\mathbf{u}}^n\approx\frac{1}{\Delta t^2}(\mathbf{u}^{n+1}-2\mathbf{u}^n+\mathbf{u}^{n-1}). \tag{7}$$

Then, substitute (6) and (7) into (5), and rearrange terms for $\mathbf{u}^{n+1}$:

$$\mathbf{u}^{n+1}=\left[2\Delta t^2\mathbf{f}^n+4\mathbf{u}^n+(c\Delta t-2)\mathbf{u}^{n-1}\right]\Big/(2+c\Delta t) \tag{8}$$

which is the update scheme for the displacement field. Equation (9) is employed to approximate $\mathbf{u}^{-1}$ to initialize the displacement iteration:

$$\mathbf{u}^{-1}=\mathbf{u}^0-\Delta t\dot{\mathbf{u}}^0+\frac{\Delta t^2}{2}\ddot{\mathbf{u}}^0, \tag{9}$$

where $\mathbf{u}^0$, $\dot{\mathbf{u}}^0$, and $\ddot{\mathbf{u}}^0$ are the initial displacement, velocity, and acceleration vector, respectively. The velocity and acceleration vectors can be updated afterwards by (6) and (7), though not necessary.

With the assumption of a unit diagonal matrix $\mathbf{\Lambda}$, the time step size needs to be selected based on Greschgorin's theorem (Kilic and Madenci, 2010), which can be written as

$$\Delta t\le\sqrt{4\Lambda_{ii}\Big/\sum\nolimits_j|K_{ij}|}, \tag{10}$$

where Λ_{ii} is the diagonal coefficients of the density matrix and K_{ij} is the stiffness matrix of the equation system. Since this stiffness matrix K_{ij} is not explicitly obtained in computing the force vector $\mathbf{f}$ (see (3) and (5)), another approximation scheme is applied for the time step size.

An appropriate time step for the one-dimensional explicit peridynamic problem is based on the wave speed c_s using the Courant–Friedrichs–Lewy (CFL) condition (LeVeque, 2007):

$$\Delta t\le 2\Delta x/c_s, \tag{11}$$

In two-dimensional cases, the CFL condition is more stringent. Assuming that the wave speeds along x and y directions are the same and the use of a uniform grid where $\Delta x=\Delta y$, the critical time step size becomes

$$\Delta t\le\Delta x\cdot\sqrt{\Lambda_{ii}/E_{\max}}, \tag{12}$$

in which $E_{\max}$ is the maximum component of the elastic stiffness matrix is used to approximate the maximum possible wave speed. Eq. (12) is the time step size employed in this paper.

The damping ratio c is then selected carefully by the lowest frequency of the system using Rayleigh's quotient (Kilic and Madenci, 2010):

$$c^n=2\sqrt{\frac{(\mathbf{u}^n)^{\mathrm{T}}\mathbf{k}^n\mathbf{u}^n}{(\mathbf{u}^n)^{\mathrm{T}}\mathbf{u}^n}}, \tag{13}$$

where $\mathbf{k}^n$ is the diagonal *local stiffness matrix*, which is given as

$$k_{ii}^n=-(f_i^n/\Lambda_{ii}-f_i^{n-1}/\Lambda_{ii})/(u_i^n-u_i^{n-1}), \tag{14}$$

where f_i^n is the ith component of the force vector $\mathbf{f}$ at time $t=n$ and Λ_{ii} is set to be 1. Since the local stiffness matrix calculation involves division by the difference between current and old displacement components, it is highly possible to encounter a zero-component in the displacement field where the criteria fails (Kilic and Madenci, 2010). Therefore, the local stiffness k_{ii}^n is set to be zero when the difference between displacement fields vanishes. Finally, an initial guess of damping ratio c_0 is given to start computation.

2.3. Numerical discretization scheme and algorithm

Assume there are N neighbor particles of the material point $\mathbf{x}$, then (3) can be discretized as (neglecting the body force $\mathbf{b}$ and only considering properties at current time t):

$$\mathbf{L}(\mathbf{x})=\sum_{i=1}^{N}\{\underline{\mathbf{T}}[\mathbf{x}]\langle\mathbf{x}_i'-\mathbf{x}\rangle-\underline{\mathbf{T}}[\mathbf{x}_i']\langle\mathbf{x}-\mathbf{x}_i'\rangle\}V_{\mathbf{x}_i'}=\mathbf{0}, \tag{15}$$

where $\mathbf{x}_i'$ is the ith particle in $\mathbf{x}$'s horizon and its corresponding volume is $V_{\mathbf{x}_i'}$. Next, the deformation gradient $\mathbf{F}(\mathbf{x})$ and shape tensor $\mathbf{K}(\mathbf{x})$ at particle $\mathbf{x}$ are discretized as the following:

$$\mathbf{F}(\mathbf{x})=\left[\sum_{i=1}^{N}\omega(\mathbf{y}_i'-\mathbf{y})\otimes(\mathbf{x}_i'-\mathbf{x})V_{\mathbf{x}_i'}\right]\mathbf{K}(\mathbf{x})^{-1},$$
$$\mathbf{K}(\mathbf{x})=\sum_{i=1}^{N}\omega(\mathbf{x}_i'-\mathbf{x})\otimes(\mathbf{x}_i'-\mathbf{x})V_{\mathbf{x}_i'}, \tag{16}$$

where $\mathbf{y}'$ and $\mathbf{y}$ are the images of $\mathbf{x}'$ and $\mathbf{x}$, respectively. Given the constitutive model, represented by an operator $\mathcal{F}$, the force state $\underline{\mathbf{T}}[\mathbf{x}]\langle\mathbf{x}_i'-\mathbf{x}\rangle$ at particle $\mathbf{x}$ can be obtained from

$$\underline{\mathbf{T}}[\mathbf{x}]\langle\mathbf{x}_i'-\mathbf{x}\rangle=\omega\mathcal{F}\big(\mathbf{F}(\mathbf{x})\big)\mathbf{K}(\mathbf{x})^{-1}(\mathbf{x}_i'-\mathbf{x}). \tag{17}$$

As for the rest half terms in (15), $\underline{\mathbf{T}}[\mathbf{x}_i']\langle\mathbf{x}-\mathbf{x}_i'\rangle$ can be obtained in a similar way, which is

$$\underline{\mathbf{T}}[\mathbf{x}_i']\langle\mathbf{x}-\mathbf{x}_i'\rangle=\omega\mathcal{F}\big(\mathbf{F}(\mathbf{x}_i')\big)\mathbf{K}(\mathbf{x}_i')^{-1}(\mathbf{x}-\mathbf{x}_i'). \tag{18}$$

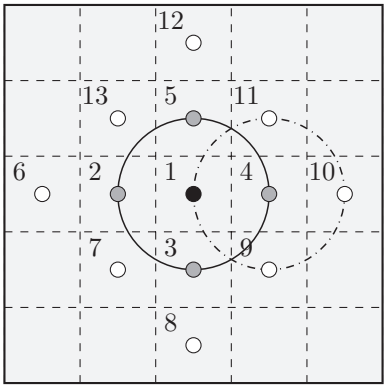

Fig. 3. Particle interactions with closest neighbors in the PD model. Particles i = 2, 3, 4, 5 are nearest neighbors of particle 1 (denoted as **x**); particles i = 1, 9, 10, 11 are nearest neighbors of particle 4 (denoted as $\mathbf{x}_i'$). In this case, all 13 particles shown above should be included in order to obtain $\mathbf{L}(\mathbf{x})$ at particle **x** in (15).

However, in order to acquire $\mathbf{F}(\mathbf{x}_i')$ and $\mathbf{K}(\mathbf{x}_i')$ at particle $\mathbf{x}_i'$, information about the ith particle's horizon needs to be known. Fig. 3 is an illustration of interactions of one particle with its nearest neighbors.

With all force vector states obtained, the adaptive relaxation dynamic method, elaborated in Section 2.2, is applied to solve the equation $\mathbf{L}(\mathbf{x}) = \mathbf{0}$. For a two-dimensional problem, the global equation of motion can be organized as a vector system with a size of $2 \times N_{\text{total}}$, where N_{total} is the total number of particles in the simulation. Since $\mathbf{L}(\mathbf{x})$ is completely dependent on the current field, the system can be explicitly started with initial guesses of displacement, velocity, and acceleration fields.

During dynamic iterations in one loading step, two absolute errors ε_1 and ε_2 are calculated at each iteration step with the definitions as

$$\varepsilon_1 = \frac{\|\mathbf{L}(\mathbf{x})\|_2}{N} \text{ and } \varepsilon_2 = \frac{\|\delta\mathbf{u}\|_2}{N}, \tag{19}$$

where l^2-norm is employed and N is the total number of particles. The first error ε_1 describes the degree to which the vector system approaches to zero while the second one ε_2 denotes the magnitude of displacement increments between two adjacent iteration steps. In order to normalize the error from initial guesses, two corresponding relative errors e_1 and e_2 are then computed and monitored, which are

$$e_1 = \frac{\varepsilon_1}{\varepsilon_1^0} \text{ and } e_2 = \frac{\varepsilon_2}{\varepsilon_2^0}, \tag{20}$$

where ε^0 is the initial absolute error in each loading step. Iterations stop only when both criteria, $e_{1,2} < e_l$, are satisfied, where $e_l = 10^{-6}$. All quantities are then updated into the next loading step.

To improve the computation performance, a parallel library, OpenMP, is adopted in the codes. Given that kinematic properties, such as the displacement **u** and deformation gradient **F**, are known before hand due to the explicit method, the constitutive model can be applied on different particles in parallel. In other words, the computation involved in acquiring $\mathbf{P}(\mathbf{x}) = \mathcal{F}\big(\mathbf{P}(\mathbf{x})\big)$ at particle **x** and $\mathbf{P}(\mathbf{x}') = \mathcal{F}\big(\mathbf{P}(\mathbf{x}')\big)$ at particle $\mathbf{x}'$ are completely independent. The computation domain is therefore partitioned into several groups with each group calculating its own stress tensor. Finally, all information is gathered in the assembly of the vector system $\mathbf{L}(\mathbf{x})$. Compared to implicit solvers, there is no matrix-inversion operation in explicit methods. Besides, this new adaptive dynamic method allows flexibility in applying different constitutive models and extending to three-dimensional cases.

3. Crystal plasticity constitutive model

The rate-independent crystal plasticity theory in Anand and Kothari (1996) is applied to model the deformation response of particles within each crystal. In the crystal lattice coordinate frame, the deformation gradient **F** can be expressed into a multiplication of the elastic $\mathbf{F}^{\text{e}}$ part and plastic $\mathbf{F}^{\text{p}}$ part, written as $\mathbf{F} = \mathbf{F}^{\text{e}}\mathbf{F}^{\text{p}}$ with $\det(\mathbf{F}^{\text{p}}) = 1$.

In the crystal plasticity theory, the plastic flow is attributed to dislocation gliding on prescribed slip systems. Assume there are N slip systems and the Schmid tensor of the αth slip system is $\mathbf{S}_0^\alpha = \mathbf{m}_0^\alpha \otimes \mathbf{n}_0^\alpha$, where $\mathbf{m}_0^\alpha$ and $\mathbf{n}_0^\alpha$ are the slip direction and normal vector at time $t = 0$, respectively. Then the plastic flow can be expressed as a summation of shearing rates on all slip systems, which is

$$\dot{\mathbf{F}}^{\text{p}}(\mathbf{F}^{\text{p}})^{-1} = \sum_\alpha \dot{\gamma}^\alpha \mathbf{S}_0^\alpha \text{sign}(\tau^\alpha), \tag{21}$$

where $\dot{\gamma}^\alpha$ and τ^α are the plastic shearing rate and resolved stress on the αth slip system, respectively.

The *conjugate stress* defined as $\bar{\mathbf{T}} = \det\mathbf{F}^{\text{e}}(\mathbf{F}^{\text{e}})^{-1}\boldsymbol{\sigma}(\mathbf{F}^{\text{e}})^{-\text{T}}$, in terms of the Cauchy stress $\boldsymbol{\sigma}$, is used to compute the resolved stress $\tau^\alpha = \bar{\mathbf{T}} \cdot \mathbf{S}_0^\alpha$ on the αth slip plane. Based on the constitutive relation, this conjugate stress can be obtained by $\bar{\mathbf{T}} = \mathcal{L}^{\text{e}}[\bar{\mathbf{E}}^{\text{e}}]$, in which $\mathcal{L}^{\text{e}}$ is the fourth-order anisotropic elasticity tensor and $\bar{\mathbf{E}}^{\text{e}}$ is the Green elastic strain, defined as $\bar{\mathbf{E}}^{\text{e}} = \frac{1}{2}(\mathbf{F}^{\text{e}\text{T}}\mathbf{F}^{\text{e}} - \mathbf{I})$.

To solve this elasto-plasticity crystal model, firstly, assume the slip system resistance on the αth slip system is s^α which works as a threshold of the resolved shear stress on the system. Only active slip systems, or those slip systems whose resolved shear stress exceed the resistance ($\tau^\alpha > s^\alpha$), have positive shearing rate ($\dot{\gamma}^\beta(t) > 0$); otherwise, there is no plastic shearing rate ($\dot{\gamma}^\beta(t) = 0$). Secondly, the slip system resistance evolves as:

$$\dot{s}^\alpha(t) = \sum_\beta h^{\alpha\beta}\dot{\gamma}^\beta(t), \text{ with } s^\alpha(0) = \tau_0^\alpha, \tag{22}$$

where $h^{\alpha\beta}$ is the hardening-coefficient matrix, $\dot{\gamma}^\beta(t) > 0$ is the plastic shearing rate on the βth slip system, and τ_0^α is the initial slip system resistance on the αth slip system.

Consequently, the plastic shear increment $\Delta\gamma^\beta$ can be solved from a matrix form (See Appendix). The plastic part of deformation gradient $\mathbf{F}^{\text{p}}$ is afterwards updated using (21) while the elastic part computed from $\mathbf{F}^{\text{e}} = \mathbf{F}(\mathbf{F}^{\text{p}})^{-1}$. In order to convert the conjugate stress $\bar{\mathbf{T}}$ into the first Piola–Kirchhoff stress **P**, the relation $\mathbf{P} = (\det\mathbf{F})\boldsymbol{\sigma}\mathbf{F}^{-\text{T}}$, or $\mathbf{P} = \mathbf{F}^{\text{e}}\bar{\mathbf{T}}(\mathbf{F}^{\text{p}})^{-\text{T}}$, should be employed with the conjugate stress computed from $\bar{\mathbf{T}} = \mathcal{L}^{\text{e}}[\bar{\mathbf{E}}^{\text{e}}]$. Finally, the slip resistance are updated at the end of each loading step using (22).

Since the equation of motion is solved by an explicit dynamic algorithm, the tangent modulus $\partial\mathbf{P}/\partial\mathbf{F}$ is not needed, which is, however, a necessary process in implicit methods, such as the Newton–Raphson's method (Sun and Sundararaghavan, 2014).

4. Numerical examples

In planar polycrystals, each grain can be characterized by a two-dimensional rotation tensor **R** which relates the local crystal lattice frame to the reference sample frame. Given an orientation θ, or the angle between crystal and sample axes, the associated rotation matrix supports parametrization as $\mathbf{R} = \cos(\theta)\mathbf{I} - \sin(\theta)\mathbf{E}$, where **E** is the two-dimensional alternator ($E_{11} = E_{22} = 0, E_{12} = -E_{21} = 1$) and **I** is the two-dimensional identity tensor. Due to planar symmetry, crystal orientations can be identified by parameters from a fundamental region $[-\pi/2, \pi/2)$, in which crystals with orientation $\theta = \pi/2$ are identical to those with $\theta = -\pi/2$.

The rotation tensor $\mathbf{R} = \mathbf{R}^e$ is evaluated through a polar decomposition of the elastic deformation gradient as $\mathbf{F}^e = \mathbf{R}^e\mathbf{U}^e$, the spin

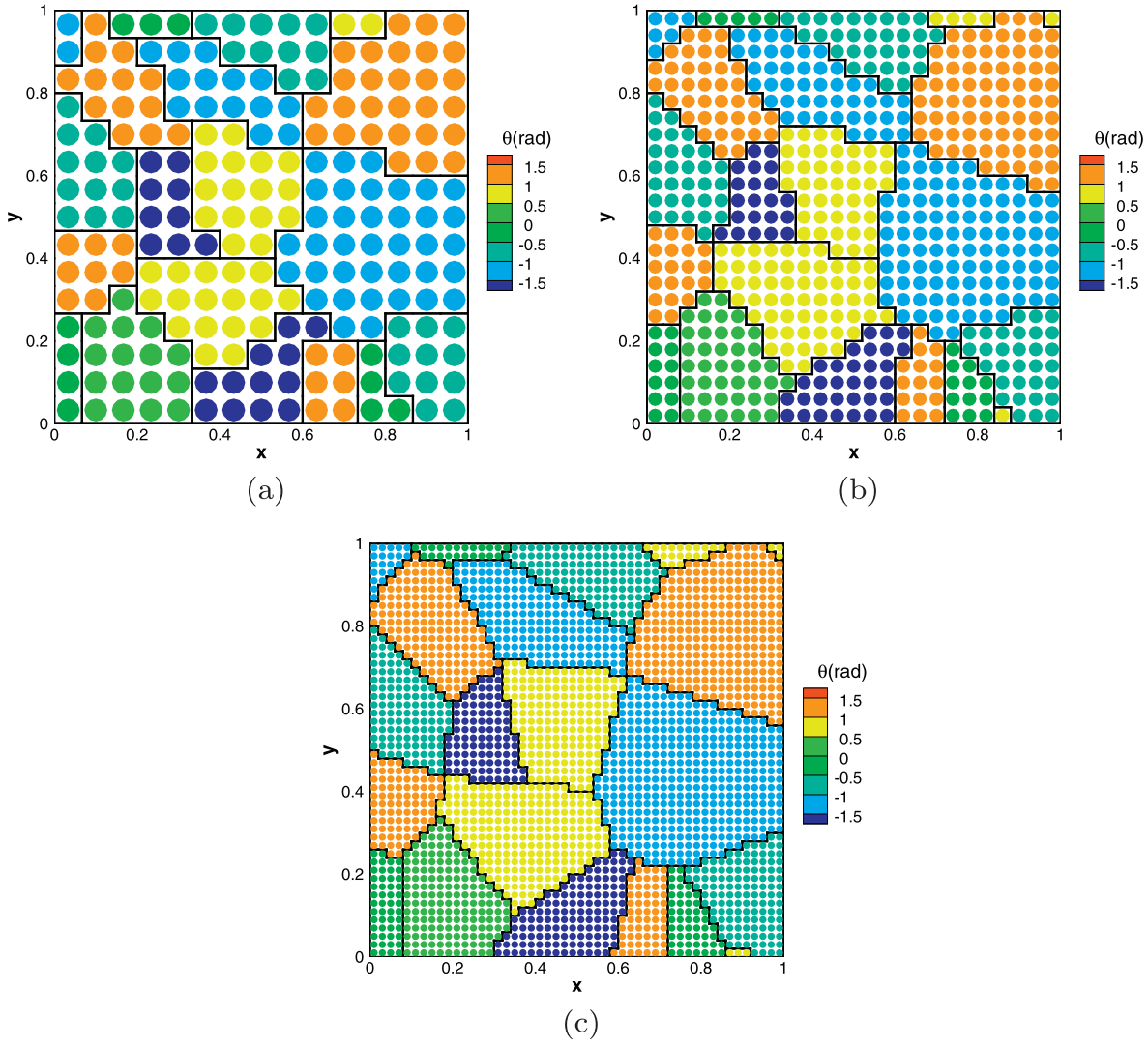

Fig. 4. Particle grids with three different mesh sizes. Orientation θ is the angle between the crystal and x axis. Particles are located at the center of elements in pixel-based grids (a) 225 particles (b) 625 particles (c) 2500 particles.

tensor $\mathbf{\Omega}$ is then defined as $\mathbf{\Omega} = \dot{\mathbf{R}}^e\mathbf{R}^{e\mathrm{T}} = -\dot{\theta}\mathbf{E}$, where $\dot{\theta} = \frac{\partial\theta}{\partial t}$ is the crystal reorientation velocity. In the component form, the crystal reorientation velocity can be expressed as $\dot{\theta} = (\Omega_{21} - \Omega_{12})/2$. Using the reorientation velocity, the crystal texturing is tracked by $\Delta\theta = \dot{\theta}\Delta t$ at each time step.

A 1×1 mm^2 polycrystalline microstructure with 21 grains, computationally generated by Voronoi construction, is considered here. The discretized computational domain is based on a pixel mesh (four-node square elements) and PD particles are located at the center of these elements. Each particle occupies a constant volume in the reference configuration equal to the area of the corresponding enclosed finite element. Twelve different orientations within the interval $[-\pi/2, \pi/2)$ are distributed with a constant step size $\pi/12$ among grains. Three particle grids based on different mesh sizes are generated and shown in Fig. 4. Two slip systems at orientations $-\pi/6$ and $+\pi/6$ are considered.

The particular hardening law in (22) is chosen as follows (Anand and Kothari, 1996):

$$h^{\alpha\beta} = h_0^{\beta}(q + (1-q)\delta^{\alpha\beta})\left(1 - \frac{s^{\beta}(t)}{s_s^{\beta}}\right)^a \text{ (no sum on } \beta), \qquad (23)$$

where h_0^{β}, $s^{\beta}(t)$, and s_s^{β} are the hardening coefficient, the current resistance, and the saturation resistance of slip system β, respectively; $\delta^{\alpha\beta}$ is the Kronecker delta function; a and q are constant terms. These hardening parameters are taken to be identical for both slip systems and are listed below:

$$h_0 = 10 \text{ MPa}, s(0) = 10 \text{ MPa}, s_s = 200 \text{ MPa}, a = 2, q = 1.4, \qquad (24)$$

where $s(0)$ is the initial slip resistance.

A displacement boundary condition is enforced on boundary particles, which is $\mathbf{u} = \left(\exp(\mathbf{L}_{\mathrm{vg}}t) - \mathbf{I}\right)\mathbf{x}$, where $\mathbf{L}_{\mathrm{vg}} = \dot{\mathbf{F}}\mathbf{F}^{-1}$ is a macroscopic velocity gradient, t is time, and $\mathbf{I}$ is the two-dimensional identity tensor. In the following examples, two different velocity gradients with the plane strain assumption are applied on microstructure boundaries to simulate the process of X-axis shear and Y-axis compression, respectively. They are

$$\mathbf{L} = \eta\begin{bmatrix} 0 & 1 \\ 1 & 0 \end{bmatrix}(\text{shear}) \text{ and } \mathbf{L} = \eta\begin{bmatrix} 1 & 0 \\ 0 & -1 \end{bmatrix}(\text{compression}), \qquad (25)$$

where $\eta = 0.0020$ is a constant strain rate. Each simulation are performed over 30 steps with the corresponding velocity gradient leading to a final strain around 0.06. The two-dimensional elastic stiffness matrix is taken as $D_{11} = 2$GPa, $D_{12} = 1$GPa, and $D_{33} = 2$GPa.

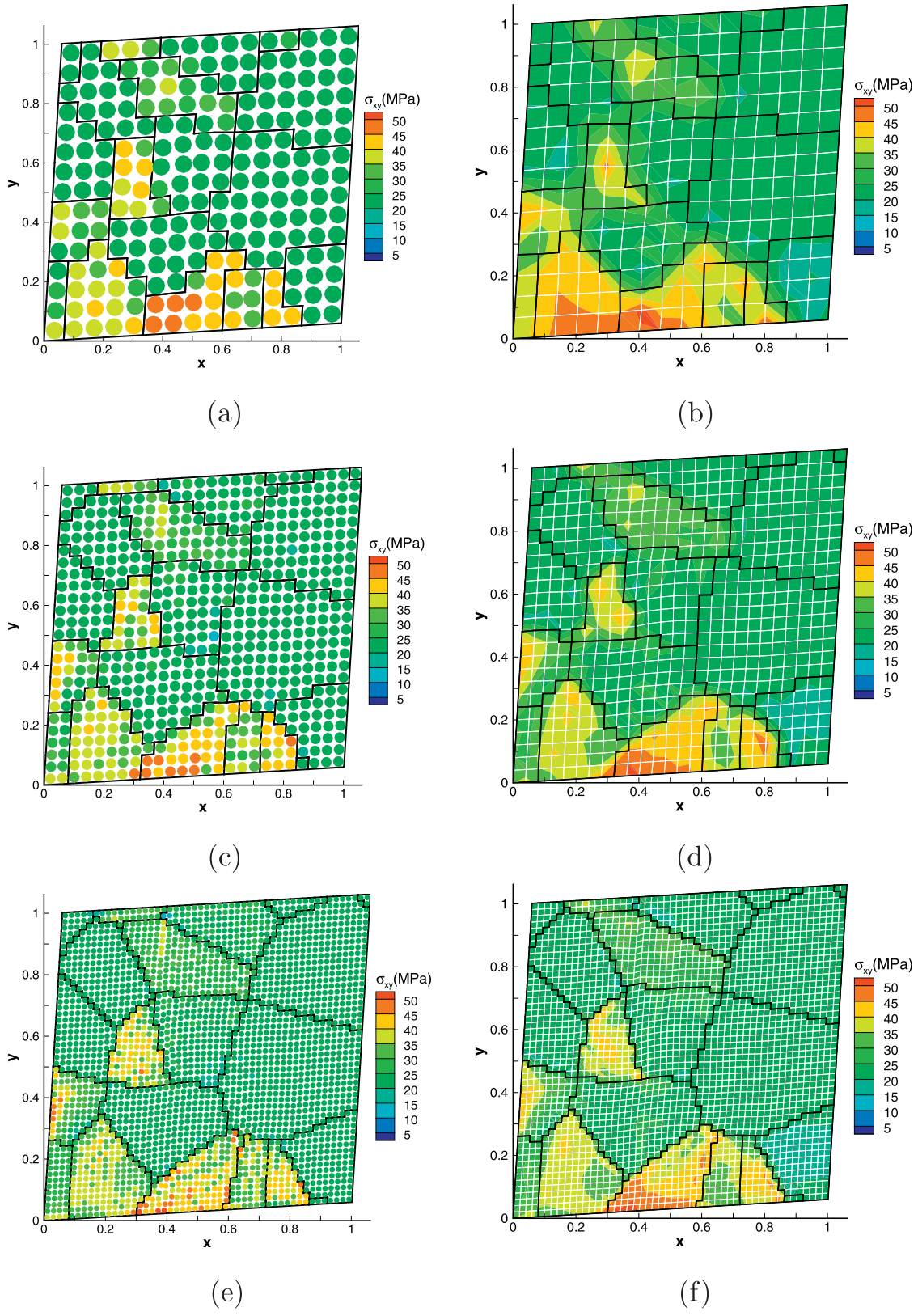

Fig. 5. Comparison of σ_{xy} from CPPD and CPFE models in the pure shear test with a 225 particles/elements mesh in (a,b), a 625 particles/elements mesh in (c,d), and a 2500 particles/elements mesh in (e,f) at total strain of 0.06.

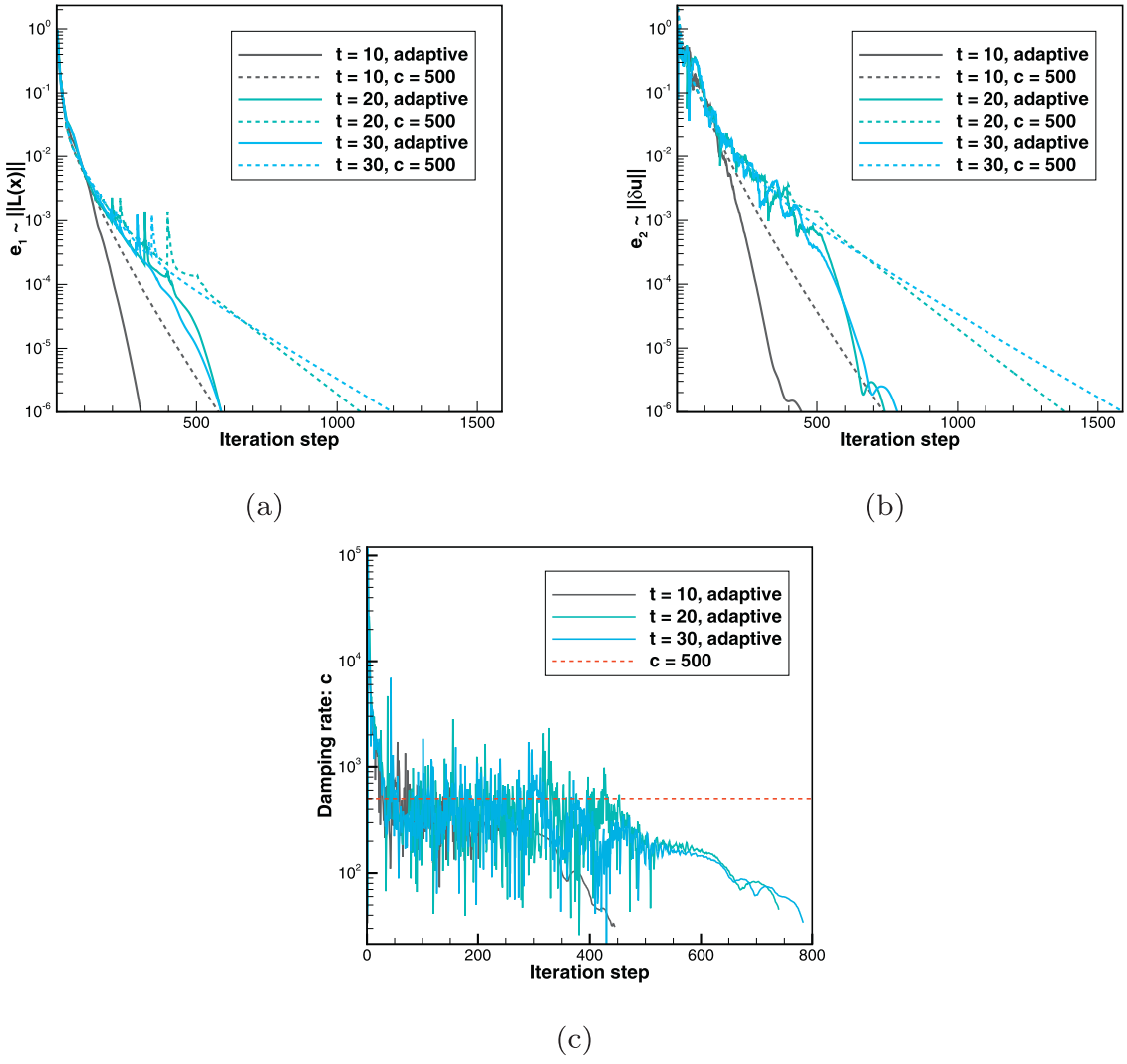

Fig. 6. The convergence plot of the dynamic CPPD model in the pure shear test with 2500 elements. Two relative errors, $e_{1,2}$, and artificial damping ratios are monitored during iterations in (a), (b), and (c), respectively, during iterations at $t = 10$, $t = 20$, and $t = 30$ (or at strain of 0.02, 0.04, and 0.06). A comparative test with a constant damping rate $c = 500$ is plotted in dashed lines.

4.1. Convergence and numerical efficiency tests in pure shear

The first test is to demonstrate the accuracy and mesh convergence of the new dynamic CPPD model. In order to compare with the CPFE model, the horizon radius in the PD model is kept minimum merely including the nearest neighbor particles and the influential function ω is set to be constant 1. With a constant influence function, the deformation gradient definition is identical to that proposed by Zimmerman et al. (2009) for modeling atomistic deformation. Although not considered in this work, one may note that the influence function can be used to play much the same role as the non-local kernel in Eringen–type (Eringen, 1983) theories. For example, the dispersion curves of the material can be modulated using different forms of ω, going from a linear dispersion in continuum limit to non–linear dispersion curves when using different influence parameters as shown in Seleson and Parks (2011). Secondly, by limiting to the nearest neighbor interactions, our formulation ensures both compatibility and traction continuity similar to the finite element problem.

Particles in the PD model are located at the center of elements in CPFE with the number of particles same as the number of elements. Linear basis functions and traditional implicit solver are employed in the CPFE model. Though different solvers are applied in CPPD and CPFE models, the same constraint on errors is set to be $e_l = 10^{-6}$. Particles in the PD simulation are colored with field values to compare with finite element contours obtained from the CPFE model. In Fig. 5, the shear stress σ_{xy} obtained from CPPD and CPFE models are compared at the final strain of 0.06 in 225, 625, and 2500 elements, respectively. The overall stress distribution and locations of maximum and minimum stresses are similar between these two models at the same degree of mesh refinement. Features of the stress response, such as the regions of stress concentration, are improved in the CPPD method as the mesh is refined.

In the case of CPPD with 2500 elements, two relative errors, $e_{1,2}$, and artificial damping ratios are monitored. Fig. 6 is the convergence plot of the dynamic CPPD model at different loading steps. Both criteria $e_1 < 10^{-6}$ and $e_2 < 10^{-6}$ are satisfied. The damping ratio oscillates dramatically in a range from 10^0 to 10^4 at the start and becomes stable towards the end. A comparative test with a constant damping ratio $c = 500$ is carried out and the adaptive dynamic relaxation method is demonstrated as converging faster and stably with the CPPD model during different loading steps in both elastic and plastic regions.

Finally, a comparison is conducted between the explicit CPPD model and implicit CPPD model from Sun and Sundararaghavan (2014). Three different mesh sizes are tested and both explicit

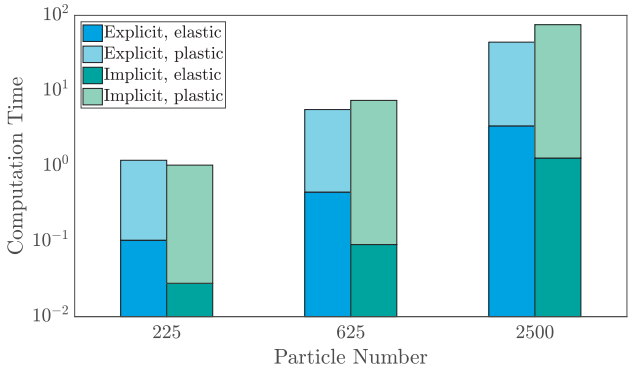

Fig. 7. Comparison of numerical efficiency between explicit and implicit CPPD models. The computation time is plotted in a log scale and normalized with the case of implicit model with 225 particles.

and implicit simulations were run in the same single-core workstation without parallelization. The absolute error ϵ_1 in (19) and relative error e_1 in (20) are monitored in both models considering that these two errors indicate the extent to which convergence is achieved. $\varepsilon_1 < 10^{-6}$ and $e_1 < 10^{-6}$ are employed to be the convergence criteria. The computation time is divided into two parts, where the first includes the first 7 loading steps when material is mainly in the elastic region and the second one contains the last 23 loading steps in the plastic region. The computational time for both models are illustrated in Fig. 7 in log-scale.

For implicit methods, computation cost is mainly spent in computing the tangent modulus and inverting the global stiffness matrix (Sun and Sundararaghavan, 2014). In contrast, the explicit method is matrix free and the speed primarily depends on the number of constitutive function calls. This explains why the implicit model is faster in the elastic region where tangent computation is avoided and it can converge in one iteration. Explicit methods are more stable and efficient in the plastic region where most of the simulation is carried out. As the particle number increases, the implicit model becomes more expensive because of repeated matrix inversion needed during convergence. In the plastic region, the explicit CPPD model's computational speed surpasses the implicit model.

4.2. Reorientation of grains and microstructural study of shear bands in a Y-axis compression test

Following is a Y-axis compression test based on the same microstructure in the previous pure shear test. Reorientation of grains predicted by CPFE and CPPD models are compared in Fig. 8 at strain of 0.06. Significant reorientation is seen within shear bands in both models. In particular, a comparison case with a horizon radius δ increased to $\sqrt{2}l_e$ and $\omega = 1$ in the CPPD model is presented to investigate the effect of horizon size on localization bands, where l_e is the minimum distance between particles. For $\delta > \sqrt{2}l_e$, the influence function needs to be modified to correctly

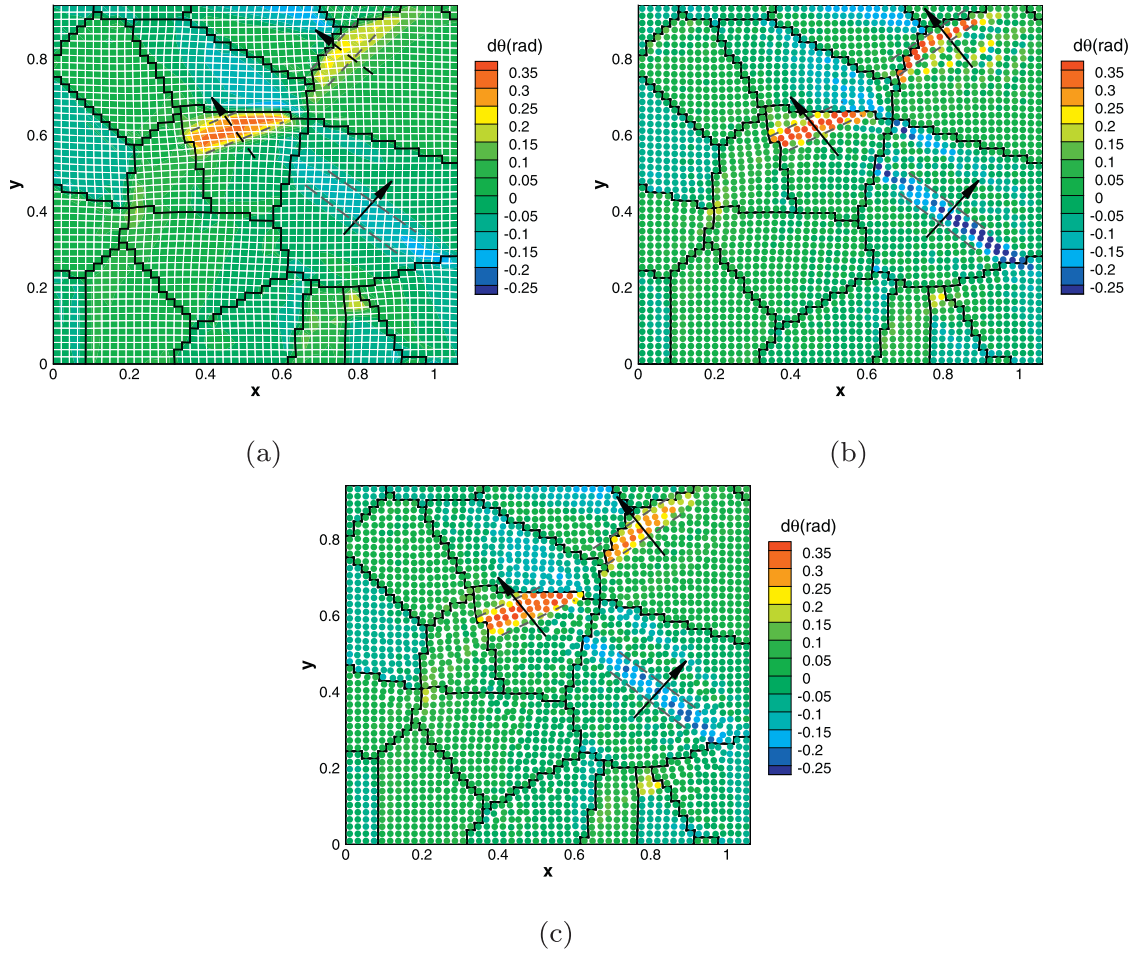

Fig. 8. Orientation changes for 2500 particles under a y-axis compression test from (a) CPFE (b) CPPD with $\delta = l_e$ (c) CPPD with $\delta = \sqrt{2}l_e$ at strain of 0.06. Along the direction of arrows, sharper and more number of shear bands can be seen in CPPD results with the smaller horizon. Use of a larger horizon radius leads to thicker shear bands, with lower reorientation intensity.

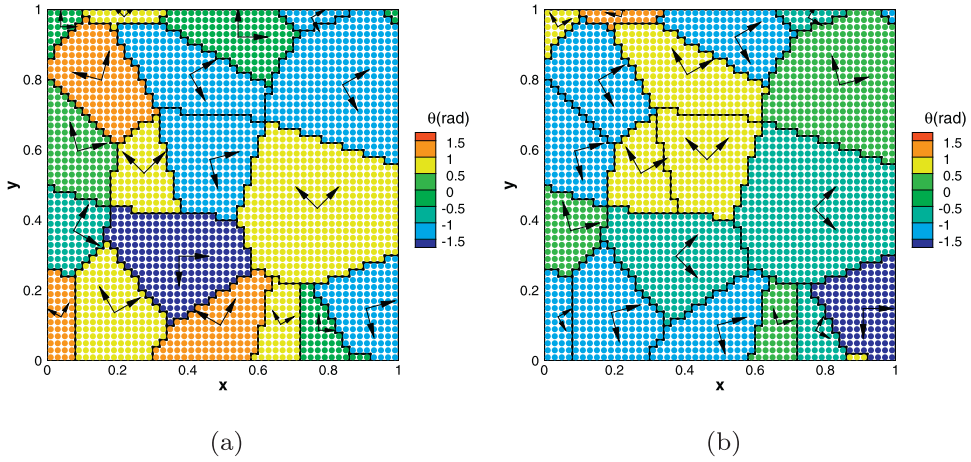

Fig. 9. Microstructures 2 and 3 represented by 21 planar grains for CPPD simulations. Initial orientations are represented by a group of two arrows. The microstructure in the pure test in Fig. 4 is employed as microstructure 1.

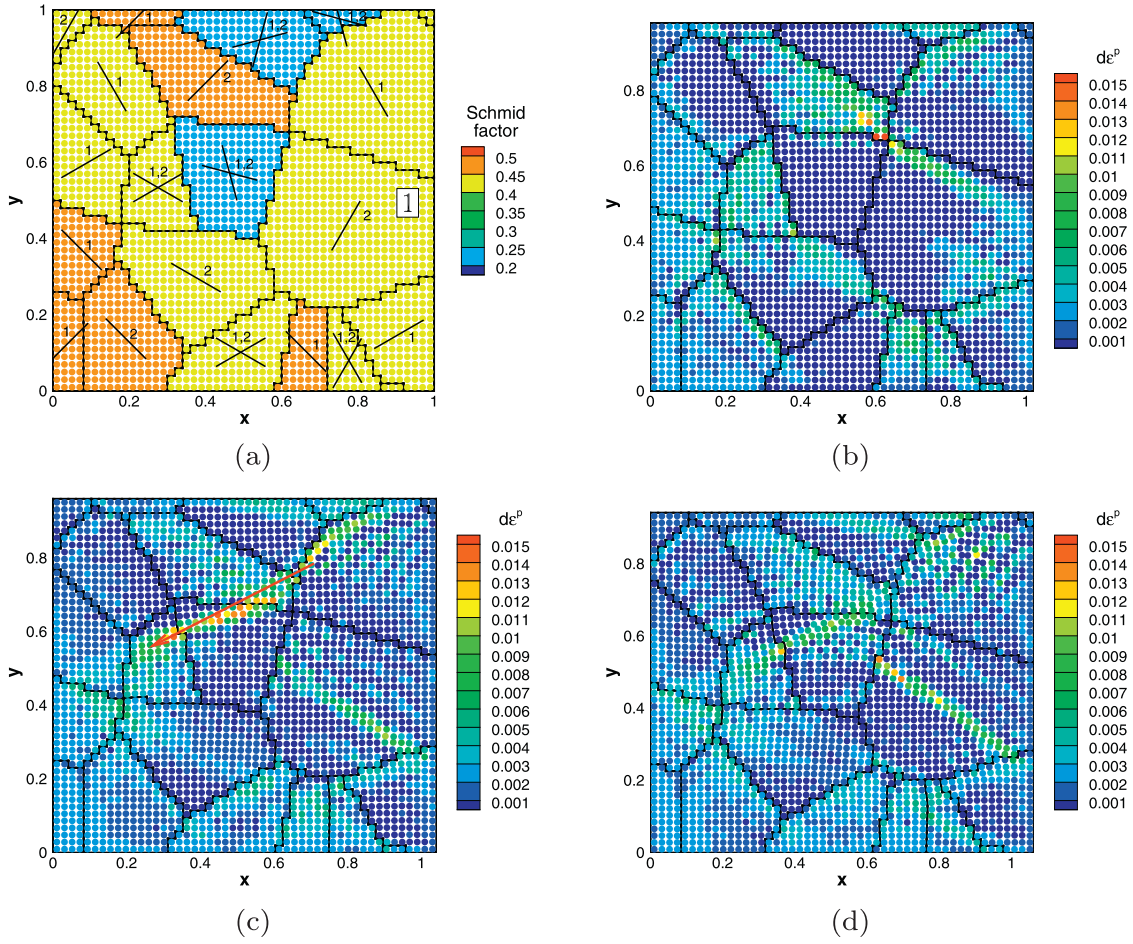

Fig. 10. Microstructure 1. (a) is the plot of the maximum Schmid factor in each grain with Grain 1 labeled. The equivalent plastic strain increment is shown in (b) at strain of 0.02, (c) at strain of 0.04, and (d) at strain of 0.06. The red arrow in (c) indicates a track of shear bands transmission across grains. (For interpretation of the references to colour in this figure legend, the reader is referred to the web version of this article.)

apply boundary conditions (Wu and Ben, 2015; Madenci et al., 2016), so the comparison is not applied in this paper.

Even though the overall contours such as the locations and orientations of shear bands of the three simulations are similar, the localization bands seen from CPFE simulations are comparatively more diffuse due to lack of an internal length scale. Along the direction of arrows in Fig. 8, the widths of shear bands obtained by CPPD simulations are smaller and their boundaries are more conspicuous for the case of the smallest horizon size. We find that increasing the horizon leads to correspondingly larger shear bands, with lower reorientation intensity. The lower intensity is due to smoothing of intense strains on a particle with lower strains from the farther particles due to non-local averaging. This example illus-

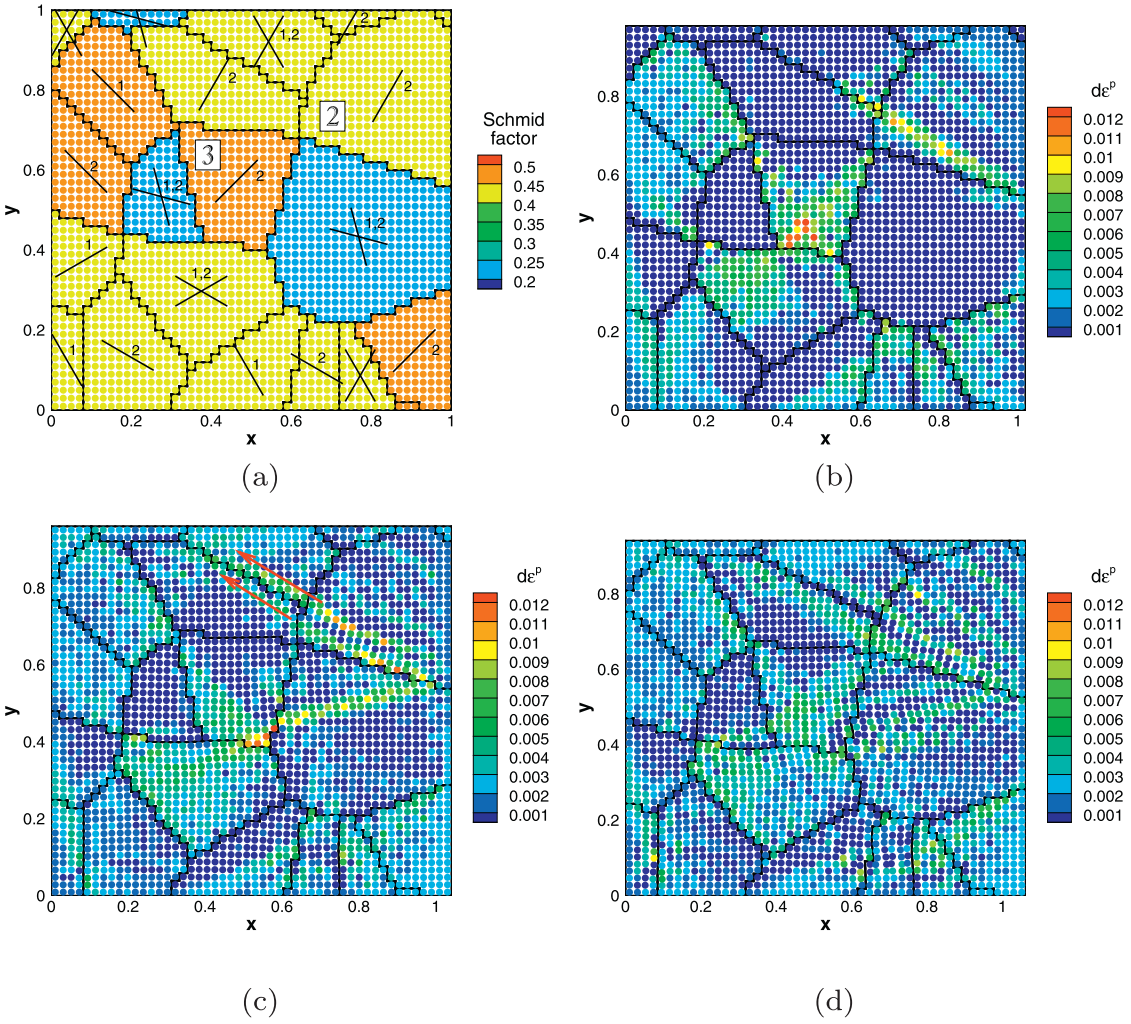

Fig. 11. Microstructure 2. (a) is the plot of the maximum Schmid factor in each grain with Grain 2 and 3 labeled. The equivalent plastic strain increment is shown in (b) at strain of 0.02, (c) at strain of 0.04, and (d) at strain of 0.06. The red arrow in (c) indicates a track of shear bands transmission across grains. (For interpretation of the references to colour in this figure legend, the reader is referred to the web version of this article.)

trates how the horizon size controls the characteristic microstructural length scale.

4.3. Study of the dependence of shear bands on initial orientation distributions

The dynamic CPPD model is used to study the origin and evolution of shear bands on three different microstructures. The first microstructure applied is identical to that of the pure test while the other two are shown in Fig. 9. The structures and positions of grains in these three microstructures stay the same, however, the orientations of grains are assigned differently. The Y-axis compression boundary condition in (25) is applied.

First off, potential active slip systems are identified using a rudimentary Schmid factor analysis. Let $\mathbf{l}_c$ and $\mathbf{l}_s$ be the loading axis in the current crystal frame and sample reference frame, respectively, and $\mathbf{l}_s = [1, 0]^T$ (or $\mathbf{l}_s = [0, -1]^T$, since their Schmid factors are the same). Then the loading axis in the current frame can be represented as $\mathbf{l}_c = \mathbf{R}^T\mathbf{l}_s$ where $\mathbf{R}$ is the rotation tensor in one crystal. Next, the Schmid factor for αth slip system is obtained by $\mathbb{S}^\alpha = |(\mathbf{m}_0^\alpha \cdot \mathbf{l}_c)(\mathbf{n}_0^\alpha \cdot \mathbf{l}_c)|$. Finally, the maximum Schmid factor is marked as the active system. Fig. 10(a), 11(a), and 12(a) are plots of the maximum Schmid factor in each grain for three different microstructures. Each grain is marked with the slip system number ($\alpha = 1, 2$) that gives the maximum Schmid factor. If the Schmid factor for both slip systems are equal, both systems are marked in one grain. In that case, to distinguish the slip system numbers, travel clockwise. Since the angle between two slip directions is always an acute angle of $\pi/3$, the first slip line encountered before the acute angle is the 2nd slip system.

Evolutions of the equivalent plastic strain increment[1] are shown as a function of the effective strain in Figs. 10–12 for three microstructures. At low strain or strain of 0.02, deformation processes primarily occur in grains with high Schmid factors while little plasticity, if any, is seen in grains with the lowest Schmid factor. As the loading is increased, strain localization emerges in the form of a laminated pattern. Consequently, a new lamellar structure is generated with plentiful fine shear bands, as shown in Figs. 10(d), 11(d), and 12(d).

During this process, shear bands are transmitted from grains with higher Schmid factors to those with lower Schmid factors and merge into larger ones. This is a possible deformation mechanism in grains not favorably oriented for slip activity (Sun and Sundararaghavan, 2014). Red arrows show the track of transmission in Figs. 10(c), 11(c), and 12(c). One particular case of slip trans-

[1] The equivalent plastic strain increment is defined as Anand and Kalidindi (1994) $d\epsilon^p = \frac{\sum_\alpha \tau^\alpha \Delta\gamma^\alpha}{\sigma_{\text{eff}}}$, where σ_{eff} is the von Mises stress.

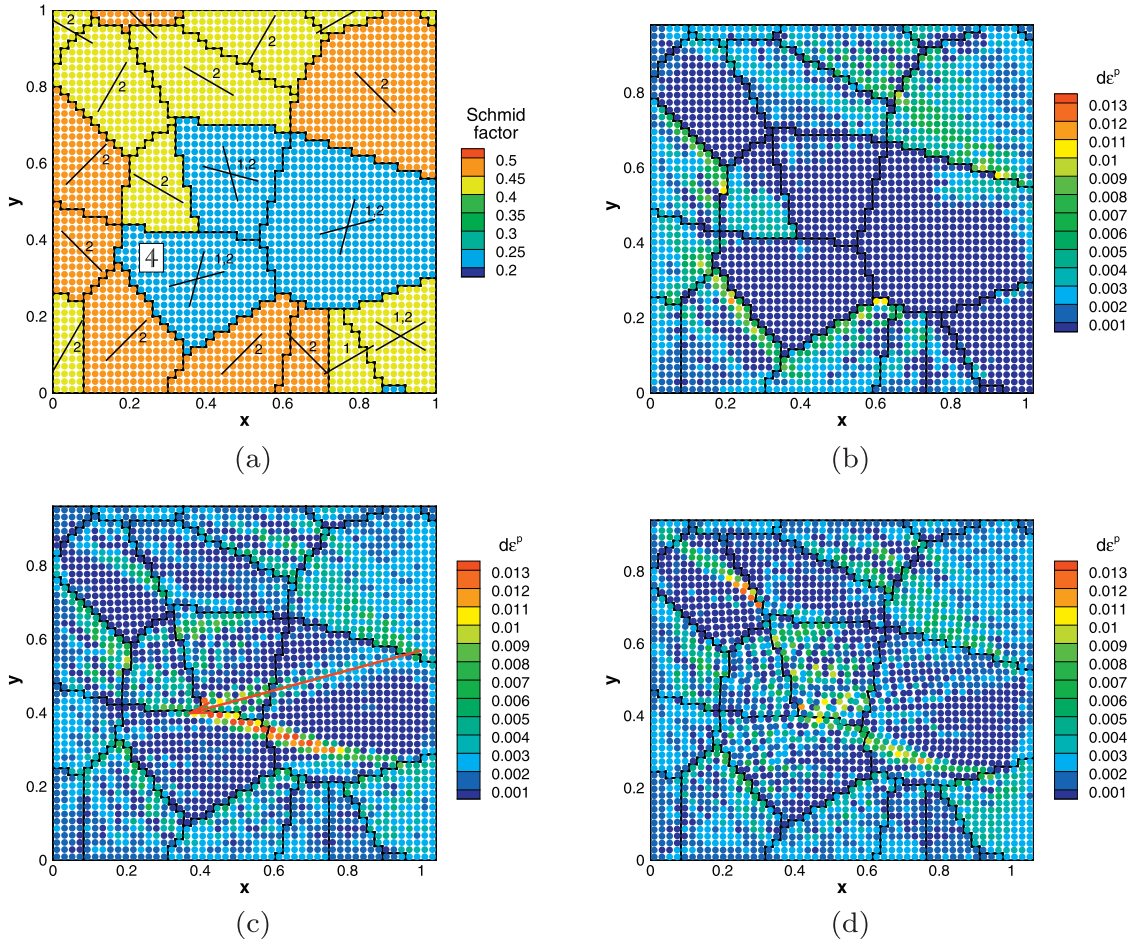

Fig. 12. Microstructure 3. (a) is the plot of the maximum Schmid factor in each grain with Grain 4 labeled. The equivalent plastic strain increment is shown in (b) at strain of 0.02, (c) at strain of 0.04, and (d) at strain of 0.06. The red arrow in (c) indicates a track of shear bands transmission across grains. (For interpretation of the references to colour in this figure legend, the reader is referred to the web version of this article.)

mission can be found in Fig. 11(c). Grain 2 in microstructure 2 and the grain to its left are grains with slip system 2 active. At higher strain, shear bands travel through grain 2 and merge into the grains to its left.

Intensified plastic strain arises across grain boundaries that separate low and high Schmid factor grains. This is due to the inability of high-Schmid-factor grains to transmit slip activity across to those grains with low Schmid factor. One example can be found at the grain boundary of Grain 3 in Fig. 11(b, c). Grain 3 is a grain with a high Schmid factor between two low-Schmid-factor grains. Another example is Grain 4 in Fig. 12(b, c, d), which is a low-Schmid-factor grain surrounded with high-Schmid-factor grains. Strong plastic strain is generated at the boundaries of these two grains, however, Grain 4 has localized strain around it rather than inside it. These grain boundaries may trigger cracks.

In order to identify the active slip systems within shear bands, maps of plastic shearing increments ($\Delta\gamma^1$ and $\Delta\gamma^2$) on slip systems 1 and 2 for Grain 1 in microstructure 1 at final strain of 0.06 are plotted in Fig. 13. Low strain is found in slip system 1 while shear bands are formed in slip system 2 as expected from the Schmid factor analysis. Particle alignments around the shear band are drawn with green lines in Fig. 13(b). The direction of alignment is the slip direction of slip system 2 in Grain 1 in Fig. 10(a), which is nearly perpendicular to the direction of the shear band. This is because dislocations are grouped along slip directions.

4.4. Stress-strain response

The homogenized stress-strain response of CPPD and CPFE models are compared in Fig. 14 for microstructures 1 and 2. The elastic responses for both models are very close, however, divergence occurs in the elasto-plastic region. The CPPD model shows an overall softer response in plastic regions, i.e., at the same strain level, the averaged stresses are lower. This is mainly due to sharper stress localizations or smaller regions with high stress in the CPPD model compared to the CPFE model.

5. Conclusions and future work

A CPPD model with an explicit adaptive dynamic relaxation method is presented in this study. A non-ordinary state-based theory of peridynamics is applied where bond forces are computed by crystal plasticity. CPPD results are compared with the CPFE analysis on plane strain problems under pure shear and compression. The mechanical properties, texturing, and stress-strain response predicted by two models are found to be largely similar. One highlight of the new dynamic CPPD model is its simplicity and numerical efficiency compared to implicit methods in the plastic regime.

In the numerical results, shear bands show inhomogeneity in the plastic deformation and reorientation. Shear bands can merge and spread into grains, which are originally unfavorable to slip at small effective strain. In the future work, three-dimensional simulations and damage models will be developed. However, a direct

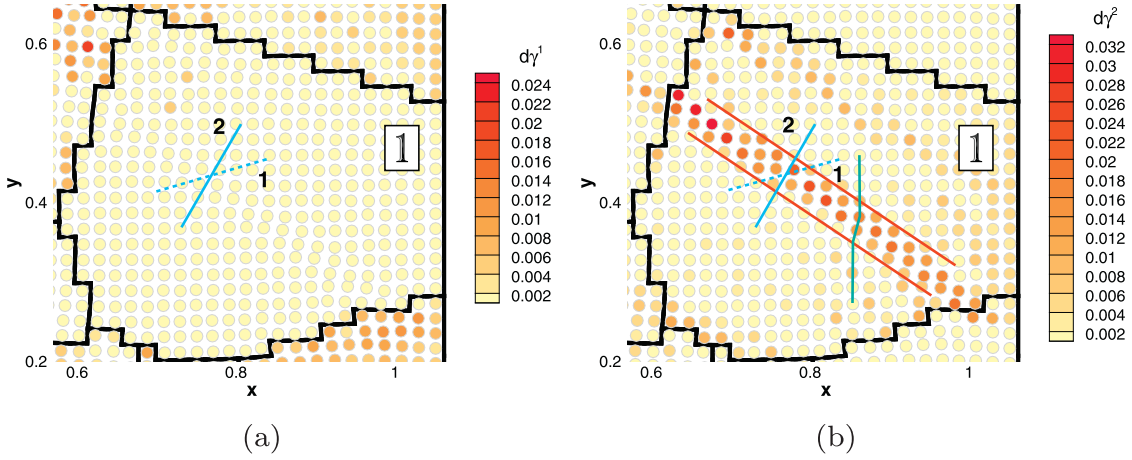

Fig. 13. Plastic shear increments in grain 1 of microstructure 1 at strain of 0.06 for (a) slip system 1 and (b) slip system 2. Blue lines denote slip directions; red lines indicate shear bands; the green line shows the particle alignment across the shear band. The direction of the particle alignment is parallel to the slip direction of slip system 2 while nearly perpendicular to the shear band. (For interpretation of the references to colour in this figure legend, the reader is referred to the web version of this article.)

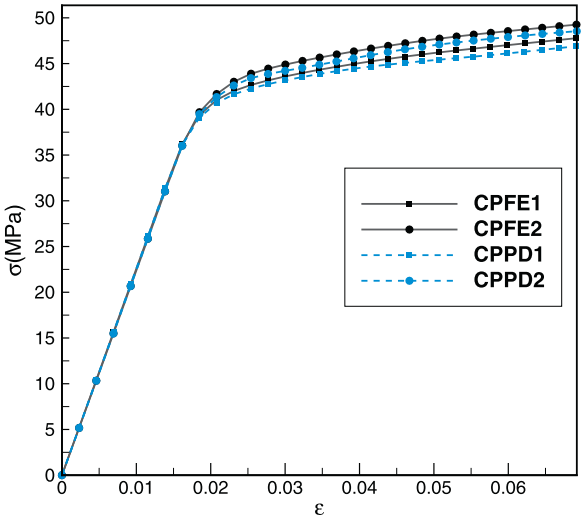

Fig. 14. Homogenized stress-strain responses from CPPD and CPFE models for microstructures 1 and 2 under Y-axis compression. CPPD stress is always lower than CPFE stress due to finer shear bands in CPPD results during plastic loadings.

implementation of damage model within the state-based peridynamics will lead to instabilities associated with unphysical diffusion of the damage zone (Tupek et al., 2013). Therefore, more sophisticated controls of instability in peridynamics needs to be employed. Finally, a parametric study with comparison to the experimental observations (Kammers and Daly, 2013; Guery et al., 2016; Dmitrieva et al., 2009) will be performed in order to understand the effect of crystal structure and deformation on the activation and propagation of shear bands more accurately.

Acknowledgment

The work presented here was funded by Office of Naval Research (ONR) grant N00014-12-1-0013. The computations have been carried out as part of research supported by the U.S. Department of Energy, Office of Basic Energy Sciences, Division of Materials Sciences and Engineering under Award no. DE-SC0008637 that funds the PRedictive Integrated Structural Materials Science (PRISMS) Center at the University of Michigan. The authors wish to thank Dr. Shang Sun for his preliminary work on crystal plasticity peridynamics.

Appendix

Constitutive update scheme

All quantities below are described in the local crystal frame. Quantities at the current time step are denoted by subscript $(n+1)$. The deformation gradient $\mathbf{F}_{n+1}$ at the current time step is known before hand. The update procedure below is applied on numerically computing the PK-I stress $\mathbf{P} = \mathcal{F}(\mathbf{F}_{n+1})$, where the operator function $\mathcal{F}$ is the constitutive model.

An Euler-backward time integration scheme for (21) leads to the following approximation with the assumption that $\Delta\gamma$ is small:

$$\begin{aligned}\mathbf{F}^{\mathrm{p}} &= \exp\Big(\Delta t \sum_{\alpha} \dot{\gamma}^{\alpha} \mathbf{S}_0^{\alpha} \mathrm{sign}(\tau^{\alpha})\Big)\mathbf{F}_n^{\mathrm{p}} \\ &\approx \Big(\mathbf{I} + \sum_{\alpha} \Delta\gamma^{\alpha} \mathbf{S}_0^{\alpha} \mathrm{sign}(\tau^{\alpha})\Big)\mathbf{F}_n^{\mathrm{p}}. \end{aligned} \tag{26}$$

Substitute (26) into the multiplicative decomposition $\mathbf{F} = \mathbf{F}^{\mathrm{e}}\mathbf{F}^{\mathrm{p}}$ and reform the equation:

$$\mathbf{F}^{\mathrm{e}} = \mathbf{F}_{\mathrm{trial}}^{\mathrm{e}}\Big(\mathbf{I} - \sum_{\alpha} \Delta\gamma^{\alpha} \mathbf{S}_0^{\alpha} \mathrm{sign}(\tau^{\alpha})\Big), \tag{27}$$

where $\mathbf{F}_{\mathrm{trial}}^{\mathrm{e}} = \mathbf{F}_{n+1}(\mathbf{F}_n^{\mathrm{p}})^{-1}$ is the trial elastic deformation gradient. At the first time step, $\mathbf{F}_0^{\mathrm{p}}$ is initialized as the identity tensor $\mathbf{I}$. The Green elastic strain measure is computed using (27) as

$$\bar{\mathbf{E}}^{e} = \frac{1}{2}\Big(\mathbf{F}^{\mathrm{e}\mathrm{T}}\mathbf{F}^{\mathrm{e}} - \mathbf{I}\Big) = \bar{\mathbf{E}}_{\mathrm{trial}}^{e} - \frac{1}{2}\sum_{\alpha} \Delta\gamma^{\alpha} \mathbf{B}^{\alpha} \mathrm{sign}(\tau^{\alpha}), \tag{28}$$

where $\bar{\mathbf{E}}_{\mathrm{trial}}^{e}$ and $\mathbf{B}^{\alpha}$ are defined as

$$\bar{\mathbf{E}}_{\mathrm{trial}}^{e} = \frac{1}{2}\Big((\mathbf{F}_{\mathrm{trial}}^{\mathrm{e}})^{\mathrm{T}}\mathbf{F}_{\mathrm{trial}}^{\mathrm{e}} - \mathbf{I}\Big), \tag{29}$$

$$\mathbf{B}^{\alpha} = (\mathbf{S}_0^{\alpha})^{\mathrm{T}}(\mathbf{F}_{\mathrm{trial}}^{\mathrm{e}})^{\mathrm{T}}\mathbf{F}_{\mathrm{trial}}^{\mathrm{e}} + (\mathbf{F}_{\mathrm{trial}}^{\mathrm{e}})^{\mathrm{T}}\mathbf{F}_{\mathrm{trial}}^{\mathrm{e}}\mathbf{S}_0^{\alpha}. \tag{30}$$

Using (28) in the constitutive relation for conjugate stress $\bar{\mathbf{T}} = \mathcal{L}^{\mathrm{e}}[\bar{\mathbf{E}}^{\mathrm{e}}]$ leads to the following:

$$\bar{\mathbf{T}} = \bar{\mathbf{T}}_{\mathrm{trial}} - \frac{1}{2}\sum_{\alpha} \Delta\gamma^{\alpha} \mathcal{L}^{\mathrm{e}}[\mathbf{B}^{\alpha}] \mathrm{sign}(\tau_{\mathrm{trial}}^{\alpha}), \tag{31}$$

where $\bar{\mathbf{T}}_{\mathrm{trial}} = \mathcal{L}^{\mathrm{e}}[\bar{\mathbf{E}}_{\mathrm{trial}}^{\mathrm{e}}]$.

A trial resolved shear stress $\tau_{\mathrm{trial}}^{\alpha} = \bar{\mathbf{T}}_{\mathrm{trial}} : \mathbf{S}_0^{\alpha}$ is then computed. A potentially active set $\mathcal{PA}$ of slip systems can be identified based on the trial resolved stress as the systems with $|\tau_{\mathrm{trial}}^{\alpha}| - s^{\alpha} > 0$.

During plastic flow, the active systems are assumed to follow the consistency condition: $|\tau^\alpha| = s^\alpha$. Increment in shearing rates $\Delta\gamma^\beta$ at each time step is obtained by solving the following equation obtained by resolving (31) along slip directions:

$$|\tau^\alpha| = s^\alpha = |\tau^\alpha_{\text{trial}}| - \frac{1}{2}\text{sign}(\tau^\alpha_{\text{trial}})\left(\sum_\beta \Delta\gamma^\beta \mathcal{L}^e[\mathbf{B}^\beta]\text{sign}(\tau^\beta_{\text{trial}})\right) : \mathbf{S}^\alpha_0, \tag{32}$$

where $\alpha, \beta \in \mathcal{PA}$.

A system of equations is obtained of the following form:

$$\sum_{\beta\in\mathcal{PA}} A^{\alpha\beta}\Delta\gamma^\beta = b^\alpha, \tag{33}$$

where

$$A^{\alpha\beta} = h^{\alpha\beta} + \frac{1}{2}\text{sign}(\tau^\alpha_{\text{trial}})\text{sign}(\tau^\beta_{\text{trial}})\mathcal{L}^e[\mathbf{B}^\beta] : \mathbf{S}^\alpha_0,$$
$$b^\alpha = |\tau^\alpha_{trial}| - s^\alpha. \tag{34}$$

If for any system $\Delta\gamma^\beta \le 0$, then this system is removed from the set of potentially active systems. The system is repeatedly solved until for all systems $\Delta\gamma^\beta > 0$.

References

Abuzaid, W., Sehitoglu, H., Lambros, J., 2013. Plastic strain localization and fatigue micro-crack formation in hastelloy X. Mater. Sci. Eng. 561 (507–519).

Anand, L., Kalidindi, S.R., 1994. The process of shear band formation in plane strain compression of fcc metals: Effects of crystallographic texture. Mech. Mater. 17 (2–3), 223–243.

Anand, L., Kothari, M., 1996. A computational procedure for rate-independent crystal plasticity. J. Mech. Phys. Solids 44 (4), 525–558.

Borst, R.D., Sluys, L.J., Mühlhaus, H.B., Pamin, J., 1993. Fundamental issues in finite element analyses of localization of deformation. Eng. Comput. 10 (2), 99–121.

Breitenfeld, M.S., Geubelle, P.H., Weckner, O., Silling, S.A., 2014. Non-ordinary state-based peridynamic analysis of stationary crack problems. Comput. Methods Appl. Mech. Eng. 272, 233–250.

Chen, B., Jiang, J., Dunne, F.P., 2017. Microstructurally-sensitive fatigue crack nucleation in ni-based single and oligo crystals. J. Mech. Phys. Solids 106, 15–33.

Dmitrieva, O., Dondl, P.W., Müller, S., Raabe, D., 2009. Lamination microstructure in shear deformed copper single crystals. Acta Mater. 57 (12), 3439–3449.

Eringen, A.C., 1983. On differential equations of nonlocal elasticity and solutions of screw dislocation and surface waves. J. Appl. Phys. 54 (9), 4703–4710.

Evers, L.P., Brekelmans, W.A.M., Geers, M.G.D., 2004. Non-local crystal plasticity model with intrinsic SSD and GND effects. J. Mech. Phys. Solids 52 (10), 2379–2401.

Gerstle, W.H., 2015. Introduction to Practical Peridynamics: Computational Solid Mechanics without Stress and Strain, 1. World Scientific Publishing Co Inc.

Guery, A., Hild, F., Latourte, F., Roux, S., 2016. Slip activities in polycrystals determined by coupling DIC measurements with crystal plasticity calculations. Int. J. Plast. 81, 249–266.

Harewood, F.J., McHugh, P.E., 2007. Comparison of the implicit and explicit finite element methods using crystal plasticity. Comput. Mater. Sci 39 (2), 481–494.

Kammers, A.D., Daly, S., 2013. Digital image correlation under scanning electron microscopy: methodology and validation. Exp. Mech. 53 (9), 1743–1761.

Khadyko, M., Marioara, C.D., Ringdalen, G., Dumoulin, S., Hopperstad, O.S., 2016. Deformation and strain localization in polycrystals with plastically heterogeneous grains. Int. J. Plast. 86, 128–150.

Kilic, B., Madenci, E., 2010. An adaptive dynamic relaxation method for quasi-static simulations using the peridynamic theory. Theor. Appl. Fract. Mech. 53 (3), 194–204.

Kuroda, M., 2011. On large-strain finite element solutions of higher-order gradient crystal plasticity. Int. J. Solids Struct. 48 (24), 3382–3394.

LeVeque, R.J., 2007. Finite difference methods for ordinary and partial differential equations: Steady-state and time-dependent problems. SIAM.

Li, S., Hao, W., Liu, W.K., 2000. Mesh-free simulations of shear banding in large deformation. Int. J. Solids Struct. 37 (48–50), 7185–7206.

Lim, H., Battaile, C.C., Carroll, J., Buchheit, T.E., Boyce, B., Weinberger, C., 2015. Multi-scale Modeling of Plasticity in Tantalum.. Technical Report. Sandia National Laboratories, Albuquerque, NM (United States).

Madenci, E., Barut, A., Futch, M., 2016. Peridynamic differential operator and its applications. Comput. Methods Appl. Mech. Eng. 304, 408–451.

Madenci, E., Oterkus, E., 2014. Peridynamic Theory and its Applications, 17. Springer.

Menzel, A., Steinmann, P., 2000. On the continuum formulation of higher gradient plasticity for single and polycrystals. J. Mech. Phys. Solids 48, 1777–1796.

Pokharel, R., Lind, J., Kanjarla, A.K., Lebensohn, R.A., Li, S.F., Kenesei, P., Suter, R.M., Rollett, A.D., 2014. Polycrystal plasticity: comparison between grain-scale observations of deformation and simulations. Annu. Rev. Condens. Matter Phys. 5, 317–346.

Ramazani, A., Abbasi, M., Kazemiabnavi, S., Schmauder, S., Larson, R., Prahl, U., 2016. Development and application of a microstructure-based approach to characterize and model failure initiation in DP steels using XFEM. Mater. Sci. Eng. 660, 181–194.

Roters, F., Eisenlohr, P., Bieler, T.R., Raabe, D., 2011. Crystal Plasticity Finite Element Methods: In Materials Science and Engineering. John Wiley & Sons.

Roters, F., Eisenlohr, P., Hantcherli, L., Tjahjanto, D.D., Bieler, T.R., Raabe, D., 2010. Overview of constitutive laws, kinematics, homogenization and multiscale methods in crystal plasticity finite-element modeling: theory, experiments, applications. Acta Mater. 58 (4), 1152–1211.

Seleson, P., Parks, M., 2011. On the role of the influence function in the peridynamic theory. Int. J. Multiscale Comput. Eng. 9 (6), 689–706.

Silling, S.A., 2000. Reformulation of elasticity theory for discontinuities and long-range forces. J. Mech. Phys. Solids 48 (1), 175–209.

Silling, S.A., Epton, M., Weckner, O., Xu, J., Askari, E., 2007. Peridynamic states and constitutive modeling. J. Elast. 88 (2), 151–184.

Sun, S., Sundararaghavan, V., 2014. A peridynamic implementation of crystal plasticity. Int. J. Solids Struct. 51 (19), 3350–3360.

Tupek, M.R., Radovitzky, R., 2014. An extended constitutive correspondence formulation of peridynamics based on nonlinear bond-strain measures. J. Mech. Phys. Solids 65, 82–92.

Tupek, M.R., Rimoli, J.J., Radovitzky, R., 2013. An approach for incorporating classical continuum damage models in state-based peridynamics. Comput. Methods Appl. Mech. Eng. 263, 20–26.

Wu, C.T., Ben, B., 2015. A stabilized non-ordinary state-based peridynamics for the nonlocal ductile material failure analysis in metal machining process. Comput. Methods Appl. Mech. Eng. 291, 197–215.

Zimmerman, J.A., Bammann, D.J., Gao, H., 2009. Deformation gradients for continuum mechanical analysis of atomistic simulations. Int. J. Solids Struct. 46 (2), 238–253.